Crustal and Uppermost Mantle Azimuthal Anisotropy beneath West and SE Brazil using Ambient Seismic Noise

Taghi Shirzad, Marcelo Assumpção, Eric Debayle, Marcelo Bianchi, Bruno Collaço, Jackson Calhau, Gabriel N Dragone, Carlos Alberto Moreno Chaves

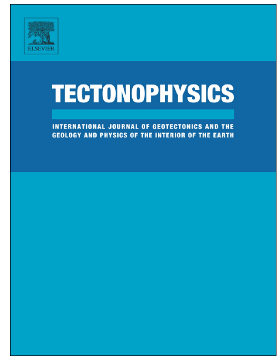

Crustal and Uppermost Mantle Azimuthal Anisotropy beneath West and SE Brazil using Ambient Seismic Noise

Taghi Shirzad, Marcelo Assumpçã, Eric Debayle, Marcelo Bianchi, Bruno Collaço, Jackson Calhau, Gabriel N. Dragone, Carlos Alberto Moreno Chaves

PII: S0040-1951(24)00238-5

DOI: https://doi.org/10.1016/j.tecto.2024.230436

Reference: TECTO 230436

To appear in: *Tectonophysics*

Received date: 11 July 2023

Revised date: 14 June 2024

Accepted date: 23 July 2024

Please cite this article as: T. Shirzad, M. Assumpçã, E. Debayle, et al., Crustal and Uppermost Mantle Azimuthal Anisotropy beneath West and SE Brazil using Ambient Seismic Noise, *Tectonophysics* (2024), https://doi.org/10.1016/j.tecto.2024.230436

Crustal and Uppermost Mantle Azimuthal Anisotropy beneath West and SE Brazil using Ambient Seismic Noise

Taghi Shirzad*[1], Marcelo Assumpção[2], Eric Debayle[3], Marcelo Bianchi[4], Bruno Collaço[5], Jackson Calhau[6], Gabriel N. Dragone[7], and **Carlos Alberto Moreno Chaves[8]**

[1] Institute of Astronomy, Geophysics and Atmospheric Sciences, University of São Paulo, São Paulo, Brazil, 05508-090. E-mail: t.shirzad@iag.usp.br; ORCID: 0000-0002-8382-4990

[2] Institute of Astronomy, Geophysics and Atmospheric Sciences; University of Sao Paulo; São Paulo, Brazil, 05508-090, marcelo@iag.usp.br , ORCID: 0000-0003-0378-8406

[3] Université Claude Bernard Lyon1, LGL-TPE, UMR 5276, ENS de Lyon, UJM Saint-Etienne, CNRS, Villeurbanne, 69100, France, eric.debayle@ens-lyon.fr; ORCID: 0000-0002-9438-7060

[4] Institute of Astronomy, Geophysics and Atmospheric Sciences, University of São Paulo, São Paulo, Brazil, 05508-090. E-mail: m.bianchi@iag.usp.br , ORCID: 0000-0002-1650-4540

[5] Institute of Astronomy, Geophysics and Atmospheric Sciences, University of São Paulo, São Paulo, Brazil, 05508-090. E-mail: bruno@iag.usp.br , ORCID: 0000-0002-3125-7971

[6] Institute of Astronomy, Geophysics and Atmospheric Sciences, University of São Paulo, São Paulo, Brazil, 05508-090. E-mail: jackson@iag.usp.br , ORCID: 0000-0001-7462-7912

7 Institute of Astronomy, Geophysics and Atmospheric Sciences, University of São Paulo, São Paulo, Brazil, 05508-090. E-mail: dragone@iag.usp.br , ORCID: 0000-0001-5054-4135

8 Institute of Astronomy, Geophysics and Atmospheric Sciences, University of São Paulo, São Paulo, Brazil, 05508-090. E-mail: calbertomc@usp.br , ORCID: 0000-0001-6414-3295

* Corresponding author: *Taghi Shirzad*

Abstract

Seismic azimuthal anisotropy within the crust and upper mantle offers important information of past and present tectonic deformation. We used ambient seismic noise to map azimuthal anisotropy in the lithosphere beneath W and SE Brazil, providing new insights into the amalgamation history of the various cratonic blocks in SW Gondwana, which are now partly buried by Phanerozoic basins. We used 72 stations from January 2016 to September 2018. To correct the non-uniform distribution of the energy flow around each inter-station path, the weighted *rms* (WRMS) stacking method was applied. The inter-station empirical Green's functions provided Rayleigh-wave group and phase velocity dispersion curves, which were used in a tomographic inversion to obtain the fast anisotropy directions, and the isotropic (mean) group and phase velocities in the period range of 4-70 s. At the shortest period, both group and phase low-velocity anomalies are observed in the sedimentary basins, while the fast direction is parallel to the deformation in the surrounding fold belts (e.g., beneath the shallow Pantanal basin). At 40 s period, group and phase velocities are affected by crustal thickness variations. During the longest period of the 70s, the fast anisotropy directions are mostly N-S, in general agreement with the azimuthal anisotropy of the global model of Debayle et al.(2016, updated to 2022), which is interpreted as due to compressional deformation in the lithospheric lid. This deformation-induced anisotropy suggests that the final Neoproterozoic collision occurred between the two groups of cratonic blocks: (*I*) the Amazon craton, the Rio Apa, and the Rio Tebicuary cratonic blocks in the Amazon domain, and (*II*) the Paranapanema block on the Atlantic domain. The isotropic V_S model generally agrees with the proposed West Paraná Suture zone (inferred from gravity and magnetotelluric data). In the lower crust (20 to 35 km), predominantly low velocities are seen in the central and southern part of the Paraná basin, and higher velocities are observed around the Pantanal basin, in general agreement with Cedraz et al. (2020) proposal of underplating in that region.

Keywords

Chaco-Paraná basin, Pantanal basin, lithospheric thinning, underplating, SW Gondwana assemblage.

1. Introduction

Global azimuthal anisotropy can explain the deformation and convective flow within the Earth's interior (e.g., Zhu et al. 2022). These patterns exhibit a broad-scale alignment with plate tectonic motion while revealing significant regional variations (e.g., Mazzullo et al. 2017). Regional seismic azimuthal anisotropy within the crust and upper mantle may reflect the preferred fault orientation (at the macroscopic scale) and lattice preferred orientation (at the microscopic scale) caused by their past and ongoing tectonic evolution (e.g., Adam and Lebedev 2012). Therefore, mapping the seismic anisotropy of the lithosphere can add valuable information to understand better the history of tectonic deformations that shaped the crust (Hao et al. 2021). In SE Brazil, both P- and S-wave seismic tomography studies have mapped the largest continental blocks and are helping to better understand the amalgamation of Western Gondwana, especially beneath large intracratonic basins such as the Paraná and Chaco basins (Fig. 1). Previous regional studies based on teleseismic P-waves (e.g., Rocha et al., 2019; Affonso et al., 2021), continental Rayleigh wave tomography (e.g., Rosa et al. 2016; Nascimento et al., 2022; 2024), and long-period S and surface waves modeling (e.g., Celli et al. 2020; Ciardelli et al. 2022), have mapped lithospheric and asthenospheric properties in SE Brazil, such as: (*I*) larger westwards extension at depth of the São Francisco craton, (*II*) a cratonic block hidden beneath the Paraná Basin (Paranapanema Block, Fig. 1), (*III*) a belt of thinned crust and lithospheric thinning along the fold belts between the major cratonic domains of the Amazon and Atlantic (Fig. 1, inset). However, none of these previous studies analyzed crustal and upper mantle anisotropy, which could add significant information about the Gondwana assemblage in this part of South America. Here, we updated the previous ambient noise tomography of Shirzad et al. (2020, 2022b) with a more effective processing and inverted for azimuthal anisotropy.

The South American continent is composed of the active Andean orogeny in the west, and the stable Precambrian platform in the center and east, as shown in the inset of Fig. 1 (e.g., Ramos 1988; Almeida et al. 2000). Archean and Proterozoic cratonic blocks are the main basement components of the platform. The large Amazon craton and the Rio Apa cratonic block (now largely buried beneath the Chaco basin) form the so called “Amazonian Domain”. The São Francisco Craton, and several other smaller cratonic blocks, such as the Paranapanema block beneath the Paraná Basin, form the “Atlantic domain” (Fig. 1, inset). The final amalgamation of these two domains by mobile belts occurred in the Neoproterozoic and Paleozoic (Almeida et al., 2000). Different models for the Paranapanema cratonic block, buried beneath the Paraná basin, have been proposed: Cordani et al. (1984) mapped a small block in the northern part of the basin using mainly geochronological data of basement samples; Mantovani et al. (2005) proposed a larger block using gravity anomalies (red dashed line in Fig. 1); slight modifications of the previous gravity-derived block was made in the tectonic map of South America (Cordani et al., 2016; dot-dashed line in Fig. 1); and Affonso et al.(2021) enlarged the block westwards based on teleseismic P-wave anomalies (pink shaded area in Fig. 1). In our study region, the large Chaco and Paraná basins are the oldest sedimentary deposits (up to 6 km thick), with subsidence starting in the Paleozoic, soon after the amalgamation of the Paranapanema block and São Francisco craton with the Amazon craton and Rio Apa block (e.g., Trindade et al., 2004). On the other hand, the origin of the recent, shallow Quaternary Pantanal Basin (only about 0.5 km deep) is debated: it could be related to the flexural effects of the Andean orogeny (e.g., Ussami et al., 1999) or to lower crust delamination processes (Cedraz et al., 2020).

Seismic anisotropy within the Earth’s uppermost mantle is often attributed to the preferred orientation of minerals like olivine. Olivine’s lattice-preferred orientation primarily contributes to the observed azimuthal anisotropy (e.g., Hansen et al., 2021). In contrast, seismic anisotropy within the crust can result from various factors. Aligned cracks (e.g., Crampin and Peacock, 2005; Adam and Lebedev, 2012), textures in metamorphic rocks (e.g., Warner et al., 2013), the presence of crystallized magma (e.g., Wu et al., 2021), deformation (e.g., Pilia et al., 2021), and sedimentary layering (Shirzad et al., 2023), all of which contribute to the observed azimuthal anisotropy. Montagner and Nataf (1986) show that the two important contributions to long-period Rayleigh wave anisotropy originate from the B and G parameters. The B has a shallow influence whereas the G has a deeper influence. Most surface wave studies consider long period surface waves (>30 s) which are less sensitive to the shallow structure. This usually causes a restriction of the anisotropic inversion at depth to 3 parameters, V_S, Gc, and Gs. In a short period range of analysis, where Rayleigh waves are more sensitive to the crustal structure, the azimuthal terms cannot be simply related to the Gc, and Gs terms, an approximation done in most studies implementing this kind of inversion. Hence, the shallow influence of the B parameters cannot be neglected and this would require inverting at depth for 5 parameters (Vsv, Bc, Bs, Gc, Gs). Thus, Mazullo et al. (2017) studies, while comprehensive in their approach, may have limitations in addressing very short periods (below 15s) where consideration of additional azimuthal terms (e.g., Bc and Bs) becomes crucial.

Previous studies (e.g., Assumpção et al., 2013; Rivadeneyra et al., 2019; Shirzad et al., 2020) showed that the crustal thickness in the Chaco and Paraná basins varies between 40-45 km, while in the Pantanal basin, it is only 30-35 km. Different geophysical methods such as gravity, magnetotellurics, and passive seismology (e.g., Chaves et al., 2016; Dragone et al. 2017, 2021; Rivadeneyra-Vera et al., 2019; Shirzad et al., 2020; Affonso et al., 2021), have been used to delineate several crustal/lithospheric blocks in our study region, but crustal seismic anisotropy has not been studied yet. Here, we used ambient seismic noise to map the Rayleigh wave azimuthal anisotropy. Our observed dispersion dataset has insufficient information to obtain simultaneously

Gc, Gs, Bc, Bs, and V_{SV} parameters. We thus restricted the local dispersion curve inversion at depth to the well resolved parameter V_{SV}, which presently lacks the capability for an in-depth inversion of azimuthal terms at shorter periods. Moreover, the calculated fast direction and isotropic term (phase and group velocity) results can provide additional information that helps to map of the lithospheric deformation properties and contributes to a better understanding of regional geodynamic evolution.

2. Data and Ambient Noise Processing

We used continuous data in central and eastern South America collected from January 2016 to September 2018 (more than 30 months; Shirzad et al. 2022b). The data was recorded by 72 broad-band seismic stations, including 35 temporary stations (XC network), 36 Brazilian RSBR network permanent stations, and one international GT station (CPUP). These stations provided a maximum of 2556 possible station pairs for the cross-correlation and retrieval of Empirical Greens Functions (EGF). After quality control, more than ~30% were rejected, and the total number of EGFs was about ~1900 for the group and ~1700 for phase velocities at 25 s period (maps of ray coverage and number of paths are shown in Figs. S1 and S2 of the Supplementary Material). We divided the continuous waveforms into an 8-hour long times series with 70% overlap, following Seats et al. (2012). All windows were normalized in time (one-bit) and frequency (whitening) domains.

2.1. Retrieving inter-station EGFs

Considering the varying azimuthal energy flow in different period bands within our study area (Shirzad et al., 2022a, 2022b), employing a single broadband period does not produce the most reliable Empirical Green's Function (EGFs). In addition, because one-bit normalization prioritizes the largest amplitudes typically associated with longer periods, standard correlations favor large periods over shorter ones.For these reasons, we applied the cross-coherency operator (Prieto et al., 2009) in three different period ranges: 4-25 s, 25-50 s, and 50-70 s. We then used the Weighted Root-Mean-Square (WRMS) stacking procedure (Shirzad et al., 2022a, 2022b). The WRMS stacking method analyzes the cross-correlation functions (CCFs) of ambient seismic noise to reduce the effect of non-uniform noise sources. This method extracts more reliable EGFs favoring (*I*) stationary noise sources, (*II*) normalized energy sources and (*III*) coherent CCF selection. Unlike classical linear stacking methods, WRMS produces EGFs that closely resemble earthquake Rayleigh waves, especially when noise sources are non-uniformly distributed. Unlike Shirzad et al. (2020), we applied a smaller period band to improve the extracted EGF signals here. We used the WRMS stacking method with the CCFs bandpass filtered with a narrow bandwidth of 2 s. For example, the CCFs were filtered in the bands 4-6s, 6-8s, 8-10s, etc. The WRMS stacking was applied to each period band. All the resulting narrow-band EGFs were then summed to get the final EGF for the 4-70s band. This approach resulted in a more than 20% increase in ray paths compared to the previous WRMS method used in Shirzad et al. (2020; 2022b).

Fig. 2 shows examples of selected EGFs at inter-station interval distances of 25, 35, and 45 km for 4-25 s, 25-50 s, and 50- 70 s, respectively. Given the high number of traces within each inter-station distance interval (up to 50 in some inter-station distance intervals), we displayed the EGFs with the highest SNR for each distance interval. This makes it easier to visualize the quality of the extracted signals within the expected signal window. Using the average of the causal and anti-causal EGFs is a standard procedure, we utilized only the direction where the EGF has higher energy (see Shirzad et al., 2020). According to Bensen et al. (2008), the azimuthal distribution of the incoming energy flow can be defined by the fraction of EGFs (ratio of the number of EGFs in each 15° azimuthal bin to the total number of EGFs). The result for each period (rose diagrams in Fig. 2) shows that the distribution of the energy flow is relatively uniform for all period ranges. The EGF energy (amplitude) in the expected signal window is between 50%-75% (the rose diagrams are normalized to 100%), implying a relatively uniform energy flow distribution despite the N-S predominance of station distributions.

2.2. Extracting dispersion curves

The observed group velocity dispersion curves, *U*, were obtained by the standard multiple filter analysis (Dziewonski, et al., 1969) with the phase-matched filter technique (Herrin and Goforth 1977). Multiple Gaussian filters were applied with variable widths according to the inter-station distance (Shapiro and Singh, 1999). We measured the group velocity dispersion using codes by Herrmann & Ammon (2013) and the far-field approximation of the Image Transformation Technique introduced and developed by Yao et al. (2006) to obtain the phase velocities, *C*. Figs. 3a and 3b show the phase and group velocity dispersion curves of all stations connecting to the RPRD station (at the eastern edge of the Pantanal Basin). The number of dispersion measurements reached 1850 for the group and 1600 for phase velocities at 26 s period. More details are shown in Fig. S2. Dispersion velocity errors vary from 0.1 km/s for short periods to ~0.6 km/s for the longest period (Fig. S2a).

3. Tomography Inversion

We first inverted all group and phase dispersion curves in a 2D tomography to produce maps, for every period, of the average velocities (V_o) and the fast directions of the azimuthal anisotropy. Subsequently, we used the isotropic component of the local group and phase velocity dispersion curves, at each geographical grid point, to invert for 1D $V_S$models. A 3D $V_S$model, composed of all 1D models, is then analyzed.

3.1. Azimuthal anisotropy

The azimuthal variation of the Rayleigh wave group and phase velocities can be expressed as (Smith and Dahlen, 1973; Montagner and Nataf, 1986):

$$V(T) = \overbrace{V_0(T)}^{isotropic-term} + \overbrace{A_1(T)cos(2\theta) + A_2(T)sin(2\theta) + A_3(T)cos(4\theta) + A_4(T)sin(4\theta)}^{anisotropic-term} \quad (1)$$

where T, and V_0 are the period, and the isotropic group or phase velocity. A_1, A_2, A_3, and A_4 are azimuthal anisotropic coefficients, and θ is the azimuth of the path with respect to the north. As explained by Debayle and Sambridge (2004), the 2θ terms contain the largest partial derivatives for the anisotropic terms of the Rayleigh waves with the 4θ terms being usually much smaller. Thus, the 4θ terms can be neglected for Rayleigh waves, and our inversion is set to calculate three unknowns $V_0(T)$, $A_1(T)$, and $A_2(T)$, at each period and each grid point. The amplitude, A, and the azimuth, Θ, of the fast direction are calculated as

$$A_{2\theta} = [A_1^2 + A_2^2]^{1/2}$$

$$\Theta_{2\theta} = tan^{-1}\frac{A_2}{A_1} \qquad (2)$$

To invert the Rayleigh wave group and phase velocity dispersion curves, we followed Debayle and Sambridge (2004). In this algorithm, the inversion regularization parameters are set by a *priori* model of standard deviation, $\sigma(r)$ (damping parameter), and a *priori* spatial correlation length l_{corr} (smoothing parameter). The function $\sigma(r)$ controls the amplitude of the model perturbation allowed at a given point r. At the same time, l_{corr} is the standard deviation of a Gaussian filter controlling horizontal smoothing of the inverted model. Fig. S3 shows the initial (background) velocity model (C_0, U_0), standard error $\sigma(r)$, regularization parameters, and number of ray paths. We used a cell size of 0.75^o for periods between 4 and 50 s and 1.0^o for periods longer than 50 s. The amount of smoothing is controlled by the parameter l_{corr}, shown in Fig. S2b, which varies from 60 km for short periods to 90 km for long periods. Debayle et al. (2016) pointed out that the inverted tomographic model is smoothed over a wavelength of about 3lcorr, corresponding to the distance between 2 grid points. Fig. 4 shows the isotropic group and phase velocity maps at periods of 8, 40, and 60 s. Fig. 5 shows the anisotropy amplitude and azimuth of the fast direction. Ray path coverages are shown in Fig. S1.

3.2. Checkerboard test

Using checkerboard resolution tests, we estimate our ability to recover the model parameters (V_0, A_1, A_2) from our dataset, ray coverage, and a priori information. Synthetic data were calculated using velocity perturbations of ±10%. The regularization parameters were the same as used with the observed data (Fig. S2). Fig. 6 shows the result of checkerboard tests for 8 s, 40 s, and 70 s. The synthetic velocity anomalies are well recovered in most of the study region, except the NE region at shorter periods due to the lower path coverage (Fig. S1). The retrieval of isotropic velocities depends on the quantity of rays crossing a cell and is not too dependent on the range of azimuths. On the other hand, the recovery of the azimuthal anisotropy requires a dense azimuthal distribution of rays within a checker cell. Therefore, using larger cells for the anisotropy test is more appropriate, especially when small-scale azimuthal results are not our focal point. According to the checkerboard test of Fig. 6, poorly resolved areas were masked in the 2D maps of Figs. 4 and 5.

3.3. 3D V_S model

The isotropic components of the group and phase velocity maps (V_0) in Fig. 4 form the dispersion curves at each grid point. Fig. 7a shows an example of a dispersion curve at grid point $\mathbf{P_1}$, depicted by the open white circle in Fig. 4 (55.5ºW 18.5ºS). For each grid point, 1D V_S profiles were obtained by inverting the phase and group dispersion curves. We used the iterative damped least-square inversion code *surf96* (Herrmann and Ammon 2013). The model was parametrized with multiple 1 km thick layers, using the initial V_S profile model of Shirzad et al. (2020), as shown by the black line in Fig.7b. In the inversion, the Moho depth was fixed from Rivadeneyra et al. (2019). The regularization parameter, based on the standard L-curve, was constant for all grid points. This parameter is a constant for the inversion procedure in all geographic grid points. The calculated 1D V_S model for grid point $\mathbf{P_1}$ is depicted by the green line in Fig. 7b. The 3D V_S model was obtained by joining all 1D profiles. Horizontal slices of V_S at depths 4, 20, 35, and 60 km are shown in Fig. 8. To enhance resolution at greater depths, we added to our inversion the Rayleigh wave group velocity dispersion curves (in the period range 50s-120s) from the continental scale tomography of Nascimento et al. (2022, 2024). For the common period range, 50 - 70s, we used the average of the two datasets with an additional smoothing of the final dispersion curve to reduce abrupt transitions in the combined curves near the 50 and 70s period. Fig. S3 shows an example of the merging of the two datasets.

3.4. Sensitivity kernel

Different periods of the Rayleigh wave sample different depth ranges. Short periods (e.g., 4 - 8 s) are generally sensitive to the upper crust, while long periods (e.g., 70 s) are more affected by structures below the crust. Sensitivity kernel functions of the fundamental mode Rayleigh group and phase velocities were calculated using the single-scattering (Born) approximations of Zhou et al. (2004). Fig. 3c shows the phase (left panel) and group (right panel) sensitivity kernels as a function of depth at the periods of 8, 40, and 70s. For each period, the depth of the maximum of the sensitivity kernel function is shown in Fig. 3d. At 8 s period, the group and phase velocities depend mainly on the V_S structure between 5 and 15 km depth. At 70 s period, the phase velocity is affected by structure in a wide depth range, mainly from 50 to 200 km with a peak sensitivity at 120 km (Fig. 3d); the group velocity, on the other hand, depends on the V_S structure within a narrower depth range of 40 - 85 km, with a peak sensitivity at 55 km.

4. Results and Discussion

4.1. Rayleigh wave 2D tomographic maps and azimuthal anisotropy

Figs. 4 and 5 show the isotropic phase and group velocities for periods 8, 40, and 70**s**, together with the fast directions from the azimuthal inversion. The difference between phase and group velocity maps is probably due to their different sensitivity kernels (Fig. 3c). At short periods (8 s, Fig. 4a,b), the phase and group velocities are consistent with the thicknesses of the sedimentary basins: lowest velocities are observed in the Paraná and Chaco-Paraná basins where total sediment thicknesses (brown contours in Figs. 4a,b) reaches 7 km (e.g., Julià et al., 2008; Dragone et al., 2017). High velocities are found beneath the Pantanal basin, where sedimentary thickness is less than about ~0.5 km, and also along the Asunción and Rio Grande arches (AA and RA in Fig. 4), which separate the Chaco and Paraná basins. The Chaco-Tarija basin with low velocity anomaly is separated from the Chaco basin in the South by the partly buried Rio Apa Block. The

Parecis basin has lower upper crustal velocities in its eastern part, where sediments are younger, consistent with studies by Nascimento et al. (2022).

At this short period, the orientations of the fast group and phase velocities are similar and have a general N-S mean direction (Fig. 5a,b). Beneath the Pantanal Basin, the fast direction is roughly parallel to the deformation in the fold belt underneath, as shown by the faults. The fast directions trend roughly NW-SE just south of the Pantanal basin and show a tendency towards SW-NE just north of the basin, following the structural trend of the Paraguay fold belt beneath the basin. This pattern could be explained by the collision between the Paranapanema block in the east, with the Rio Apa block (RAB) and Amazon Craton in the west during the Neoproterozoic assemblage of west Gondwana.

In the central and northern parts of the Paraná basin, the crustal anisotropy is weaker but seems to show a slight trend towards the E-W direction. Beneath the Ponta Grossa Arch (PGA; around 24°S and 51°W), the fast direction seems to change to NW-SE, parallel to the swarm of Mesozoic magmatic dykes indicated by the thin red lines (emplaced during the South Atlantic rifting). However, the anisotropy parameters in the Ponta Grossa arch are not well resolved (Fig. 6), and a better ray path coverage will be necessary in the future to confirm this apparent trend.

At 40 s period (Fig. 5), the isotropic velocity is affected by the lower crust and the upper mantle. The largest amplitudes of the sensitivity kernels range from ~25 to 60 km (Figure 3c), which limits tectonic interpretation. Beneath the northern part of the Paraná basin, the lower velocities (Figs. 4c,d) are probably due to the thicker crust (> 40 km). In areas where the crust is thinner (35 km or less), the velocities are higher as they are influenced by the mantle.

At 60s period, the most striking feature is the low velocity trend beneath the Pantanal and Chaco basin, to the west of the Western Paraná Suture. This is probably due to the thin lithosphere in that region as mapped by Ciardelli et al. (2022) and Nascimento et al. (2024). Long period (60 s, Fig. 4) group velocity samples the uppermost mantle mainly around 58 km depth, while phase velocity is sensitive to a wider depth range below the crust (Figs. 3c and 3d). Several features observed in the 40 s isotropic velocities are still present at 60s.

At 70s (Fig. 5c,d) the degree of anisotropy is about half that of the crustal layers. The general mean N-S trend of the fast group-velocity direction agrees with the fast S_V direction (green bars, Fig. 5e) of the recent 3D global model 3DLGL-TPESv.v2022-11 by Debayle et al. (2016, updated in 2022/11, here after abbreviated as "3D2022Sv") for 70 km depth, and could be interpreted as anisotropy in the shallow part of the continental lid. Because of its broader sensitivity kernel, phase velocity directions (Fig. 5c) likely reflect anisotropy both in the deep crust and uppermost mantle. This may explain the poorer agreement with the N-S anisotropy directions of the model 3D2022Sv. Group velocities at 70 s, on the other hand, are mainly sensitive to depths of 40-85 km (Fig. 3c), and so are more consistent with upper mantle anisotropy mapped by 3D2022Sv (Debayle et al., 2016) at 70 km depth (Fig. 5e).

Our predominantly N-S group-velocity fast directions, however, are not in agreement with the generally ~E-W SKS fast direction (Melo and Assumpção, 2018), as shown in Fig. 5f. In fact, the SKS fast directions agree very well with Debayle's fast direction at ~200 km depth. This could confirm that the observed SKS fast directions are mainly due to mantle flow near the lithosphere/asthenosphere boundary, as Melo and Assumpção (2018) inferred. Our mainly N-S fast direction for group velocities at the 70s period, consistent with Debayle's fast direction at 70 km, could then be interpreted as due to frozen anisotropy in the shallow part of the lithospheric lid. (also called "vertically coherent deformation" by Silver, 1966). This N-S fast direction could be explained by the E-W convergence between the two groups of cratonic blocks: (*I*) Paranapanema Block and Rio de La Plata craton on the Atlantic domain, and (*II*) Amazon craton, Rio Apa block and also the "Rio Tebicuary craton" on the Amazonian domain. Interestingly, Dragone et al.(2017, 2021) used gravity and MT data to propose that the buried Rio Tebicuary craton would be a separated unit from the Rio de La Plata craton, which is usually considered to encompass most part of the Chaco basin basement (e.g., Rapela et al., 2007). Our anisotropy results suggest that the proposed Rio Tebicuary cratonic block should be part of the Amazon domain.

4.2 3D Model and Crustal Properties

4.2.1. Upper crust

Horizontal slices of our 3D model, composed of all 1D inverted V_S profiles, are shown in Fig. 8 at shallow crust (4 km depth), middle and lower crust (20 and 35 km), and upper mantle (60 km). Fig. 9 shows three E-W vertical profiles across our study area. At 4 km depth (Fig. 8b), V_S as low as 3.3 km/s are seen in the basins, especially in the deep northern part of the Paraná basin, Chaco-Tarija and Chaco basins, probably due to smearing effects between sediments and crystalline upper crust. Areas of average to high V_S in the upper crust are seen beneath the thin (~0.5 km deep) Pantanal basin and along the Asuncion and Rio Grande arches.

Woldemichael (2003) interpreted low gravity anomalies and low resistivity data as a basement composed of metasedimentary rocks beneath the western part of the Pantanal basin (stippled area in Fig. 9a). At 4 km depth (Fig. 8b), V_S is lower in the NW part of the basin compared with the SE part, consistent with Woldemichael's (2003) interpretation. In addition, an East dipping fault zone was also proposed beneath the Pantanal basin (black wedge in profile AA' of Fig.9), which is roughly consistent with the V_S contrasts at mid crustal depths that could indicate upward motion of the eastern block.

4.2.2 Middle Crust

Dragone et al.(2017) proposed a suture between the Paraná block on the East and the Rio Apa Craton + Pantanal basement on the West, based on high/low crustal density contrast between West/East. This Western Paraná Suture ("WPS" depicted by the dark green lines in Figs. 8c,d,e) is consistent with the contrast between mid crustal V_S in the northern part of our study region. Using high resistivities in the crust and upper mantle (Bologna et al., 2019; Dragone et al., 2021) and a new interpretation of gravity anomalies, Dragone et al.(2021) revised the location of the WPS extending it southwards (red line in Figs. 8c,d,e). The revised WPS now separates high mantle V_S beneath the Paraná basin from average to low V_S beneath the Chaco basin (Fig. 8e), which is more consistent with the resistivity models.

4.2.3 Lower Crust and Underplating

Joint inversion of receiver functions and group-velocity dispersion by Cedraz et al. (2020) revealed distinct types of crustal structure in our study region. Beneath the Pantanal basin, thin crust (about 35 km thick, with normal V_S in the lower crust) was found mainly in the Eastern part of the basin (white tringles in Fig. 8d). This is generally in agreement with our V_S contours in the vertical profile of Fig. 9a. High velocity layers in the lower crust (labeled “HVL”) were also found beneath several stations around the Pantanal basin, as shown by the blue triangles in Fig. 8d (35 km depth slice). Normal velocities in the lower crust were found for all stations in the Paraná basin (red triangles in Fig. 8d). This pattern is generally consistent with our V_S anomalies in the lower crust: HVL stations are predominantly in areas of high V_S, and the lower crust in the Paraná basin has generally low velocities.

4.2.3. Lithospheric thinning

The uppermost mantle beneath the Pantanal, Chaco-Tarija, and Chaco basins, west of WPS, is characterized by low Vs, as indicated by the horizontal slice at 60 km depth (Fig. 8e). This low velocity region has been mapped before as a lithospheric thin belt, both by global and continental scale tomography models (e.g., Priestley et al., 2018; Ciardelli et al., 2022). This lithospheric thinning (“LT”) shows up as low velocities in the three E-W profiles of Fig. 9.

This lithospheric thinning can be traced from central Brazil, roughly along the Transbrasiliano belt, through the Pantanal basin (e.g., Rocha et al., 2011; 2019), and seems to be a characteristic of the limit between the Amazonian and Atlantic cratonic domains. The southward extension of this lithospheric thinning, together with the N-S fast velocities of the azimuthal anisotropy cast some doubt on the extension of the LTB to the SW (seen in Fig. 1, inset), as inferred in the last South America tectonic map (Cordani et al., 2016), and used to separate the Amazonian from the Atlantic cratonic domains.

5. Conclusions

A combination of the global (GT), permanent (BL, BR, ON), and temporary (XC) seismic networks allowed us to study the crustal and upper mantle azimuthal anisotropy. Improved processing of the ambient noise data allowed retrieval of a larger number of Rayleigh-wave EGFs. 2D inversion showed good resolution of the isotropic component and the fast direction of the azimuthal anisotropy in the center part of our study region. Anisotropy patterns in the crust and lithospheric lid are studied for the first time in the region of the Chaco-Paraná and Pantanal regions.

In the upper crust, both the dispersion and the inverted Sv velocities reflect the deep Chaco-Tarija, Chaco, and Paraná sedimentary basins. The two major basins (Chaco and Paraná) are separated by areas of normal to high velocities in the upper crust along the Rio Grande and Asunción arches. In the upper crust, the trend of NW-SE and N-S fast azimuthal directions is interpreted as due to crustal deformation in the fold belt beneath the Pantanal basin (Paraguay fold belt) as well as between the Paranapanema block on the East and the Rio Apa and Rio Tebicuary cratonic blocks on the west. This fold belt, surrounding the southern border of the Amazon craton, marks the last episode of amalgamation in SW Gondwana in the Neoproterozoic.

In the middle and lower crust (20 - 35 km), two regions are seen with different patterns: normal to low V_S (<= 4 km/s at ~35 km depth) beneath the Paraná basin, and high V_S beneath and around the Pantanal basin in the NW. This confirms the results of Cedraz et al. (2020). Generally low V_S in the lower crust of the Paraná basin also reinforces the hypothesis that underplating (possibly related to the Mesozoic magmatism and continental rifting) is not widespread in the basin, but restricted to a few locations, as suggested by Juliá et al. (2088) and An et al. (2024). The location of the Western Paraná Suture, proposed by Dragone et al. (2021) based on gravity and resistivity anomalies, is in rough agreement with our model: E-W density/velocity contrast at crustal levels across the border between the Paraná and Pantanal basins, and high resistivity/velocity contrast in the lithospheric lid in the southern part of the Paraná basin.

In the lithospheric lid, a belt of low V_S was found extending from the Pantanal basin, in the north, towards the south beneath the Chaco basin. This is consistent with a belt of thin lithosphere seen in previous global and continental surface-wave tomography. The general N-S direction of the fast velocities, observed at 70 s, is consistent with the regional pattern of the 3D global model of Debayle et al. (2016, version 2022.11) at 70 km depth. This is best interpreted as due to compressional deformation arising from the E-W convergence of cratonic blocks in the last amalgamation of SW Gondwana, which implies that the Rio Tebicuary cratonic block is best placed in the Amazon domain, casting doubt on the inferred continuation of the Transbrasiliano Lineament in the Chaco basin as separating those two domains.

6. Data and Resources

The XC data (temporary deployment) was supported by FAPESP project 2013/24215-6. Data from the permanent Brazilian networks (BR, BL, and ON) are open at www.rsbr.gov.br. XC data can be shared upon request to the Seismology Center (http://www.sismo.iag.usp.br) of the University of São Paulo. Data from seismic station CPUP is available at http://ds.iris.edu/mda/GT/CPUP. The updated version of the "3D2022Sv" global model (3DLGL-TPESv.v2022-11 by Debayle et al., 2016) is available at IRIS https://ds.iris.edu/ds/products/emc-3dlgl-tpesv.

7. Declaration of Competing Interests

The authors acknowledge there are no conflicts of interest recorded.

8. Acknowledgments

T.S. thanks the Fundação de Apoio à Universidade de São Paulo, FUSP, [project number 3930], and Fundação de Amparo à Pesquisa do Estado de São Paulo (FAPESP), Brazil [grant number 2016/20952-4]. *E.D.* is supported by the French ANR JIGSAW2 ANR- 20-CE49-0001-01. All plots were made using *Generic Mapping Tools* (*GMT*), version 6.4.0 (Wessel and Smith, 1998; www.soest.hawaii.edu/gmt, last accessed June 2024). All processing and simulations were performed using a cluster system of the Institute of Astronomy, Geophysics and Atmospheric Sciences (IAG; www.iag.usp.br) of the University of São Paulo (USP). We would also like to thank the Editor, *Dr. Claire A. Currie*, and two anonymous reviewers for their constructive comments and useful suggestions.

9. Authors contributions

Taghi Shirzad: Conceptualization, Methodology, Software, Validation, Formal analysis, Investigation, Writing - Original Draft & Editing, Visualization

Marcelo Assumpção: Conceptualization, Validation, Writing - Original Draft & Editing, Supervision, Project administration

Eric Debayle: Methodology, Software, Writing - Editing Draft

Marcelo Bianchi: Validation, Investigation, Resources, Data Curation

Bruno Collaço:, Validation, Investigation, Resources, Data Curation

Jackson Calhau: Resources, Data Curation

Gabriel N. Dragone: Discussion, Investigation, Editing, Visualization

Carlos Alberto Moreno Chaves: Discussion, Editing

10. References

Adam, J. M.-C., Lebedev, S., 2012. Azimuthal anisotropy beneath southern Africa from very broad-band surface-wave dispersion measurements. *Geophysical Journal International*, 191, 155–174, doi: 10.1111/j.1365-246X.2012.05583.x

Affonso, G. M. P. C., Rocha, M. P., Costa, I. S. L., Assumpção, M., Fuck, R. A., Albuquerque, D. F., Portner, D. E., Rodríguez, E. E., Beck, S.,L., 2021. Lithospheric architecture of the

Paranapanema Block and adjacent nuclei using multiple-frequency *P*-wave seismic tomography. *Journal of Geophysical Research: Solid Earth*, *126*, e2020JB021183. https://doi. org/10.1029/2020JB021183

Almeida, F.F.M.D., B.B.D. Brito Neves, and C.D.R. Carneiro (2000). The origin and evolution of the South American Platform, *Earth-Sci. Rev.*, 50(1–2), 77–111. https://doi.org/10.1016/S0012-8252(99)00072-0

An, M., M. Feng, M. Assumpção, M.B. Bianchi,G.S. França, M.P. Rocha, L. Sánchez Bettucci, (2024). Influence of upwelling mantle magmas on cratonic-crust implied from *V*p/*V*s beneath South America platform. *Tcctonophysics*, revised version submitted.

Assumpção, M., M. Feng, A. Tassara, and J. Julià (2013). Models of crustal thickness for South America from seismic refraction, receiver functions and surface wave tomography, *Tectonophysics*, 609, 82–96. https://doi.org/10.1016/j.tecto.2012.11.014

Batte, A. G., A. Schumann, and E. M. Twesigomwe (2021). Seismic anisotropy accrued by seven unusually deep local earthquakes (between 50 and 60 km) in the Albertine Rift: implications of asthenospheric melt upwelling. *Journal of Seismology*, 25, 921–936. https://doi.org/10.1007/s10950-021-10007-2

Bensen, G.D., M. H. Ritzwoller, & N. M. Shapiro (2008). Broadband ambient noise surface wave tomography across the United States, *J. Geophys. Res.*, 113, B05306, doi:10.1029/2007JB005248.

Bologna, M.S., Dragone, G.N., Muzio, R., Peel, E., Nuñez-Demarco, P. & Ussami, N. (2019). Electrical structure of the lithosphere from Rio de la Plata Craton to Paraná Basin: amalgamation of cratonic and refertilized lithospheres in SW Gondwanaland. Tectonics, 38, 77–94. https://doi.org/10.1029/2018TC005148

Cedraz, V., J. Julià, and M. Assumpção (2020). Joint Inversion of ReceiverFunctions and Surface-WaveDispersion in the Pantanal Wetlands:Implications for Basin Formation. *Journal of Geophysical Research:* , 125, e2019JB018337. https://doi.org/10.1029/2019JB018337

Celli, N.L., Lebedev, S., Schaeffer, A.J., Ravenna, M. and Gaina, C. (2020). The upper mantle beneath the South Atlantic Ocean, South America and Africa from waveform tomography with massive data sets. *Geophysical Journal International*, *221*(1), pp.178-204.

Chaves, C., N. Ussami, and J. Ritsema (2016), Density and P-wave velocity structure beneath the Parana Magmatic Province: Refertilization of an ancient lithospheric mantle, *Geochem. Geophys. Geosys*t., 17, 3054–3074, doi:10.1002/2016GC006369.

Ciardelli, C., Assumpção, M., Bozdağ, E. and van der Lee, S. (2022). Adjoint waveform tomography of South America. *Journal of Geophysical Research: Solid Earth*, *127*(2), p.e2021JB022575.

Cordani, U. G., B. B. Brito Neves R. A. Fuck, R. Porto, A. Thomas Filho, and F. M. B. Cunha (1984). Estudo Preliminar da Integração do Pré-Cambriano com os Eventos Tectônicos das Bacias Sedimentares Brasileiras, Série Ciência-Técnica-Petróleo, vol. 15, 70 pp., PETROBRAS, Rio de Janeiro, Brazil.

Cordani, U., V. Ramos, L.M. Fraga, M. Cegarra & I.Delgado (2016). Tectonic Map of South America. Published by CPRM (Brazilian Geological Survey), 2nd edition.

Crampin, S., S. Peacock (2005). A review of shear-wave splitting in the compliant crack-critical anisotropic Earth. *Wave Motion*, 41, 59–77. doi:10.1016/j.wavemoti.2004.05.006

Debayle, E., and M. Sambridge (2004), Inversion of massive surface wave data sets: Model construction and resolution assessment. *J. Geophys. Res*., 109, B02316, doi:10.1029/2003JB002652.

Debayle, E., F. Dubuffet, and S. Durand (2016). An automatically updated S-wave model of the upper mantle and the depth extent of azimuthal anisotropy. *Geophys. Res. Lett*., 43(2), 674–682. https://doi.org/10.1002/2015GL067329

Dragone, G.N., N. Ussami, M.E. Gimenez, F.G. Lince Klinger, and C.A.M. Chaves (2017). Western Paraná suture/shear zone and the limits of Rio Apa, Rio Tebicuary and Rio de la Plata Cratons from gravity data, *Precambrian Res*., 291, 162–177. https://doi.org/10.1016/j.precamres.2017.01.029

Dragone, G.N., Bologna, M. S., Ussami, N., Giménez, M.E., Alvarez, O., Klinger, F.G.L., Correa-Otto, S. (2021). Lithosphere of South American intracratonic basins: Electromagnetic and potential field data reveal cratons, terranes, and sutures, *Tectonophysics*, 811, 228884. https://doi.org/10.1016/j.tecto.2021.228884

Dziewonski, A., S. Bloch, M. Landisman, (1969). A technique for the analysis of transient seismic signals. *Bull. Seismol. Soc. Am.* 59 (1), 427–444. https://doi.org/10.1785/BSSA0590010427.

Hansen, L. N., M. Faccenda, and J. M. Warren (2021). A review of mechanisms generating seismic anisotropy in the upper mantle. *Physics of the Earth and Planetary Interiors* , 313, 106662. https://doi.org/10.1016/j.pepi.2021.106662

Hao, S., Z. Huang, C. Han, L. Wang, M. Xu, N. Mi, and D. Yu (2021). Layered crustal azimuthal anisotropy beneath the northeastern Tibetan Plateau revealed by Rayleigh-wave Eikonal tomography. *Earth and Planetary Science Letters*, 563, 116891. https://doi.org/10.1016/j.epsl.2021.116891

Herrin, E.E., and T.T.Goforth (1977). Phase-matched filters: Application to the study of Rayleigh Waves, *Bull. Seism. Soc. Am.*, 67, 1259–1275. https://doi.org/10.1785/BSSA0670051259

Herrmann, R.B., and C. J. Ammon (2013). Computer programs in seismology – surface waves, receiver functions and crustal structure, Saint Louis University. Available at: http://www.eas.slu.edu/People/RBHerrmann/ComputerPrograms.html.

Julià, J., M. Assumpção and M.P. Rocha (2008). Deep crustal structure of the Paraná Basin from receiver functions and Rayleigh-wave dispersion: Evidence for a fragmented Cratonic root. *J. Geophys. Res.*, 113, B08318, doi:10.1029/2007JB005374.

Mantovani, M. S. M., M. C. L. Quintas, W. Shukowsky, and B. B. Brito Neves (2005). Delimitation of the Paranapanema block: A geophysical contribution. *Episodes*, 28, 18–22.

Mazzullo, A., Stutzmann, E., Montagner, J. P., Kiselev, S., Maurya, S., Barruol, G., & Sigloch, K. (2017). Anisotropic tomography around La Réunion island from Rayleigh waves. *Journal of Geophysical Research* , 122(11), 9132-9148.

Melo, B.C., M. Assumpção (2018). Mantle anisotropy and asthenospheric flow around Cratons in Southeastern South America. *Geophys. J. International*, 215, 494-506. https://doi.org/10.1093/gji/ggy288.

Milani, E.J., Faccini, U.F., Scherer, C.M., Araújo, L.M., Cupertino, J.A. (1998). Sequences and stratigraphic hierarchy of the Paraná Basin (Ordovician to Cretaceous), Southern Brazil. *Boletim IG USP*, Série Científica, n. 29.

Montagner, J. P., Nataf, H. C. (1986). A simple method for inverting the azimuthal anisotropy of surface waves. *Journal of Geophysical Research*, 91(B1), 511-520, https://doi.org/10.1029/JB091iB01p00511

Nascimento, A. V. d. S., G. S. França, C. A. M. Chaves, and G. S. Marotta (2022). Rayleigh wave group velocity maps at periods of 10–150 s beneath South America, *Geophys. J. Int*. 228(2), 958-981. doi: 10.1093/gji/ggab363.

Nascimento, A.V.S., G.S. França, C.A.M. Chaves, G.S. Marotta, and M. Assumpção (2024). Unraveling Precambrian cratonic roots beneath South America: a contribution from surface wave tomography. *Geophys. J. Int.*, submitted (in revision).

Pilia, S., A. Kaviani, M. P. Searle, P. Arroucau, M. Y. Ali, and A. B. (2021). Crustal and mantle deformation inherited from obduction of the Semail ophiolite (Oman) and continental collision (Zagros). *Tectonics*, 40, e2020TC006644. https://doi.org/10.1029/2020TC006644.

Prieto, G. A., J. F. Lawrence, and G. C. Beroza (2009). Anelastic Earth structure from the coherency of the ambient seismic field. *Journal of Geophysical Research*, 114, B07303, doi:10.1029/2008JB006067.

Priestley, K., McKenzie, D., & Ho, T. (2018). A lithosphere-asthenosphere boundary-a global model derived from multimode surface-wave tomography and petrology. In H. Yuan, & B. Romanowicz, (Eds.), *Lithospheric discontinuities*, p 111–123. American Geophysical Union. https://doi.org/10.1002/9781119249740.ch6

Ramos, V. A. (1988). Late Proterozoic-Early Paleozoic of South America- A Collisional History. *Episodes*, 11(3), 168-174, https://doi.org/10.18814/epiiugs/1988/v11i3/003

Rapela, C.W., Pankhurst, R.J., Casquet, C., Fanning, C.M., Baldo, E.G., González-Casado, J.M., Galindo, C. and Dahlquist, J. (2007). The Río de la Plata craton and the assembly of SW Gondwana. *Earth-Science Reviews*, *83*(1-2), pp.49-82.

Rivadeneyra-Vera, C., M. Bianchi, M. Assumpção, V. Cedraz, J. Julià, M. Rodríguez., L. Sánchez, et al. (2019). An updated crustal thickness map of central South America based on receiver function measurements in the region of the Chaco, Pantanal, and Paraná Basins, southwestern Brazil. *J. Geophys. Res*, 124.doi: /10.1029/2018JB016811

Rocha, M. P., M. Schimmel, & M. Assumpção (2011). Upper-mantle seismic structure beneath SE and Central Brazil from P- and S-wave regional traveltime tomography. *Geophysical Journal International*, 184(1), 268–286. https://doi.org/10.1111/j.1365-246X.2010.04831.x

Rocha, M.P., M. Assumpção, G. M. P. C. Affonso, P. A. Azevedo, and M. Bianchi (2019). Teleseismic P-wave tomography beneath the Pantanal, Paraná and Chaco-Paraná Basins, SE South America: Delimiting lithospheric blocks of the SW Gondwana assemblage, *J. Geophys. Res.*, 124(7), 7120–7137. https://doi.org/10.1029/2018JB016807

Rosa, M. R., Collaço, B., Assumpça, M., Sabbione, N., Sanchez, G. (2016). Thin crust beneath the Chaco-Parana Basin by surface-wave tomography, J*ournal of South American Earth Sciences*, 66, 1-14, http://dx.doi.org/10.1016/j.jsames.2015.11.010

Seats, J.K., J.F. Lawrence, and A. G. Prieto (2012). Improved ambient noise correlation functions using Welch's method. *Geophys. J. Int*. 188, 513–523. https://doi.org/10.1111/j.1365-246X.2011.05263.x

Shapiro, N. M., and Singh, S. K. (1999). Short note: A systematic error in estimating surface-wave group-velocity dispersion curve and a procedure for its correlation. *Bull. Seismol. Soc. Am.*, 89 (4), 1138-1142.

Shirzad, T., Assumpção, M., Bianchi, M. (2020). Ambient seismic noise tomography in West-Central and Southern Brazil: Characterizing the crustal structure of the Chaco-Paraná, Pantanal and Paraná Basins. *Geophys. J. Int*., 220 (3), 2074-2085; https://doi.org/10.1093/gji/ggz548

Shirzad, T., Assumpção, M., Collaço, B., Calhau, J., Bianchi, M.B., Barbosa, J.R., Prieto, R.F., Carlos, D.U., 2022a. Shear wave velocities in the upper crust of the Quadrilátero Ferrífero, Minas Gerais: Rayleigh-wave tomography, *Brazilian J. Geophys*., 40 (2), 1-23, 10.22564/brjg.v40i2.2160

Shirzad, T., Safarkhani, M., Assumpção, M., 2022b. Extracting reliable empirical Green's functions using weighted cross-correlation functions of ambient seismic noise in West-Central and Southern Brazil. *Geophys. J. Int*., DOI: 10.1093/gji/ggac126

Shirzad, T., YaminiFard, F., Naghavi, M., 2023. Near-surface azimuthal anisotropy using the Rayleigh wave inversion in the Tehran region, Iran. J. Seismol, 27, 901–917. https://doi.org/10.1007/s10950-023-10169-1.

Silver, P.G., 1996. Seismic anisotropy beneath the continents: probing the depths of geology, *Annu. Rev. Earth Planet. Sci*., 24(1), 385–432.

Smith, M.L., and F.A. Dahlen (1973). The azimuthal dependence of Love and Rayleigh wave propagation in a slightly anisotropic medium. *J. Geophys. Res*., 78, 3321–3333. https://doi.org/10.1029/JB078i017p03321

Trindade, R.I.F., M. S D'Agrella-Filho, M. Babinski, E. Font, and B.B. Brito Neves (2004). Paleomagnetism and geochronology of the Bebedouro cap carbonate: evidence for continental-scale Cambrian remagnetization in the São Francisco Craton, Brazil. *Precambrian Research*, 128 (1–2), 83-103. https://doi.org/10.1016/j.precamres.2003.08.010

Ussami, N., S. Shiraiwa, and J. M. L. Dominguez (1999). Basement reactivation in a sub-Andean foreland flexural bulge: The Pantanal wetland, SW Brazil. *Tectonics*, 18(1), 25-39. https://doi.org/10.1029/1998TC900004

Warner, M., A. Ratcliffe, T. Nangoo, J. Morgan, A. Umpleby, N. Shah, V. Vinje, I. Štekl, L. Guasch, C. Win, G. Conroy, and A. Bertrand (2013). Anisotropic 3D full-waveform inversion. *Geophysics*, 78(2), 59–80, doi:10.1190/GEO2012-0338.1

Woldemichael, S.F., 2003. Estruturas Geoelétricascrustais da Bacia do Pantanal e Faixa Paraguai: implicações tectônicas. *PhD thesis*, Instituto de Astronomia, Geofísica e CiênciasAtmosféricas, Universidade de São Paulo, SP, Brasil, 189 p.

Wu, C., T. Xu, Y. Ai, W. Dong, L. Li, J. Hou (2021). Crustal azimuthal anisotropy in the Jiaodong Peninsula: Evidence for the suture between the North China Craton and South China Block. *Physics of the Earth and Planetary Interiors*, 314, 106705. https://doi.org/10.1016/j.pepi.2021.106705

Yao, H., R.D. Van Der Hilst, and M.V. De Hoop (2006). Surface-wave array tomography in SE Tibet from ambient seismic noise and two-station analysis – I. Phase velocity maps. *Geophys. J. Int*. 166, 732–744. http://dx.doi.org/10.1111/j.1365- 246X.2006.03028.x.

Yin X., Xia, J., Shen, C., Xua, H., 2014. Comparative analysis on penetrating depth of high-frequency Rayleigh and Love waves, *Journal of Applied Geophysics*, 111, 86–94. https://doi.org/10.1016/j.jappgeo.2014.09.022

Zhou, Y., Dahlen, F.A., Nolet, G., 2004. Three-dimensional sensitivity kernels for surface wave observables, *Geophys. J. Int*., 158, 142–168. https://doi.org/10.1111/j.1365-246X.2004.02324.x

Zhu, H., Yang, J., Li, X., 2020. Azimuthal Anisotropy of the North American Upper Mantle Based on Full Waveform Inversion, *Journal of Geophysical Research*, 125(2), e2019JB018432, https://doi.org/10.1029/2019JB018432

Fig. 1. Simplified geology of the study region. The 72 broadband stations (triangles)include permanent stations of the Brazilian network (sub-nets BL, BR and ON), one international station (US), and temporary deployments (XC). Pink areas are exposed cratons or buried cratonic blocks (dashed contours). Three models of the Paranapanema Block, beneath the Paraná basin, are shown: thick dashed line = based on gravity data (Mantovani et al., 2005), dot-dashed = slight modification by Cordani et al.(2016), and pink area = from P-wave tomography (Affonso et al., 2021). Gray areas are Neoproterozoic fold belts, and yellow are intracratonic basins; PtB = Pantanal Quaternary basin. AA and RGA are the Asuncion and Rio Grande arches separating the Chaco from the Paraná basins. PGA is the Ponta Grossa arch. Dark gray lines are faults from the CPRM (2016) database. Green lines are country borders. INSET: Red lines indicate the major cratons; blue line separates the Andean orogeny from the stable platform; brown line is the Transbrasiliano Lineament (TBL) separating the two cratonic domains: Amazonian and Atlantic.

Fig. 2 Selected inter-station EGF signals as function of inter-station distances at period bands of 4-25s (**a**) every 25 km, 25-50s (**b**) every 35 km, and 50-80s (**c**) every 45 km. The expected signal window is shown by dashed black lines, corresponding to velocity range between 2.5-5.0 km/s. The rose-diagrams show the normalized distribution of energy flow as a function of azimuth of the inter-station path with 15° azimuthal bins (only EGFs with SNR≥ 10 were used).

Fig. 3. All phase (**a**) and group (**b**) velocity dispersion curves connected with RPRD station. (**c**) normalized sensitivity kernel functions of phase (left panel) and group (right panel) velocities for 8s period (solid gray line), 40s (dashed gray line), and 70s (solid black line). (**d**) The depth (as a function of period) corresponding to the maximum of the sensitivity kernel.

Fig. 4. Rayleigh wave phase, *C*, (left) and group, *U*, (right) isotropic velocities for 8s. Ray path coverages are in Fig. S1. Areas with poor resolution (Fig.6) are not shown. The white circle is the grid point $\mathbf{P_1}$ (55.5ºW 18.5ºS). a, b) T = 08s: brown contours are sedimentthickness (Milani et al. 1998). c, d) T = 40s: brown contours are crustal thickness (updated from Assumpção et al., 2013, and Rivadeneyra et al., 2019) at 35 and 40 km.

The dark green line is the Western Paraná Suture of Dragone et al. (2017). Other symbols as in Fig. 1.

Fig. 5. Rayleigh wave fast azimuthal directions (blue bars) from the 2D inversion of phase (**a**, **c**) and group (**b**, **d**, **e**, **f**) velocities. At T=8 s (**a**, **b**), sampling the upper crust, the fast directions seem to follow the structural grain of the fold belt beneath the Pantanal basin; towards the Ponta Grossa Arch (PGA) the fast directions seem to align with Mesozoic dykes (redlines). At T=70s (**c** to **f**), sampling the upper mantle, our observed fast directions trend mainly N-S west of the Paraná suture (green lines). (**e**) This general N-S direction (blue bars) is consistent with the global model 3D2022Sv of Debayle et al. (2016, updated to 2022), shown by green bars. (**f**) The SKS fast average polarization directions (red bars, Melo et al., 2018) trend WSW-ENE beneath the Pantanal region, and WNW-ESE south of the Paranapanema block, consistent with fast direction of model 3D2022Sv at 200km, but different from our observed azimuthal directions (blue bars).

Fig. 6. Recovered phase (left), *C*, and group (right), *U*, velocities and fast directions from checkerboard resolution test for periods 8, 40 and 60 s. The forward problem had velocities U_0±10% and alternating N-S and E-W fast directions. The red plus symbols (+) are the limits of the synthetic fast direction anomalies (changes from NS to EW). Light gray

lines are country borders. The black lines are the limits of well resolved areas for the isotropic V_S.

Figure 7

Fig. 7 (**a**) Isotropic local group, *U*, and phase, *C*, dispersion curves at grid point P_1 (55.5ºW 18.5ºS). (**b**) calculated 1D isotropic V_S model (green line) at grid point P_1. The initial 1D V_S model (black) at this grid was taken from Shirzad et al. (2020). Solid lines in (**a**) are the inverted dispersion curves of the output model (green) in b).

Figure 8

Fig. 8 Geological map and horizontal depth slices of V_S anomaly. The black solid and dashed lines show the basins and cratonic blocks, respectively. White lines in the 4 km depth are thickness contours of the Paraná sedimentary basin. The green and red lines in the 20 - 60 km depth are the two versions of the Western Paraná Suture (WPS, Dragone et al., 2017; 2021). In the 35 km slice, the colored triangles denote lower crust type from Cedraz et al.(2020): blue = high velocity lower crust, red = normal lower crust (Vs<= 3.8 km/s), white = thin crust ~35 km. White lines in the 60 km slice locate the vertical profiles of Fig. 9. Other symbols as in Fig. 1.

Fig. 9 Isotropic V_S model for three profiles A-A' (at 18.0º S), B-B' (at 22.6º S), and C-C' (at 27.2º S) shown in Fig. 8. The thick dashed line is the Moho depth (updated from Assumpção et al. 2013 and Rivanedeyra et al., 2019). In profile AA', the stippled zone are meta-sediments (between 57.5^o-55.5^{o}W, and depth up to ~8 km) and the black "wedge" is a suture zone modeled byWoldemichael (2003). AC = Amazon Craton, Pt = Pantanal basin, Pb = Paraná basin, and WPS = Western Paraná Suture. "Underplating" and HVL in profile AA' denotes high V_S lower crust interpreted as underplating by Cedraz et al. (2019). In profile CC' lower *Vs* in the lithospheric mantle is due to lithospheric thinning ("LT") extending from the Pantanal Basin in the north to the Rio de La Plata region in the south, as seen in the tomography models such as Ciardelli et al.(2022) and Nascimento et al.(2024).

Declaration of interests

☒The authors declare that they have no known competing financial interests or personal relationships that could have appeared to influence the work reported in this paper.
The authors declare the following financial interests/personal relationships which may be considered as potential competing interests:

Highlights

- In the upper crust, azimuthal anisotropy is aligned with fold belts; at the lithospheric mantle, it is due to orogenic compressional deformation.

- Crustal V_S anomalies support the proposed N-S suture zone between the Paranapanema block and the southern part of the Amazonian craton.
- High V_S in the lower crust confirms probable underplating in the southern part of the Amazon craton.

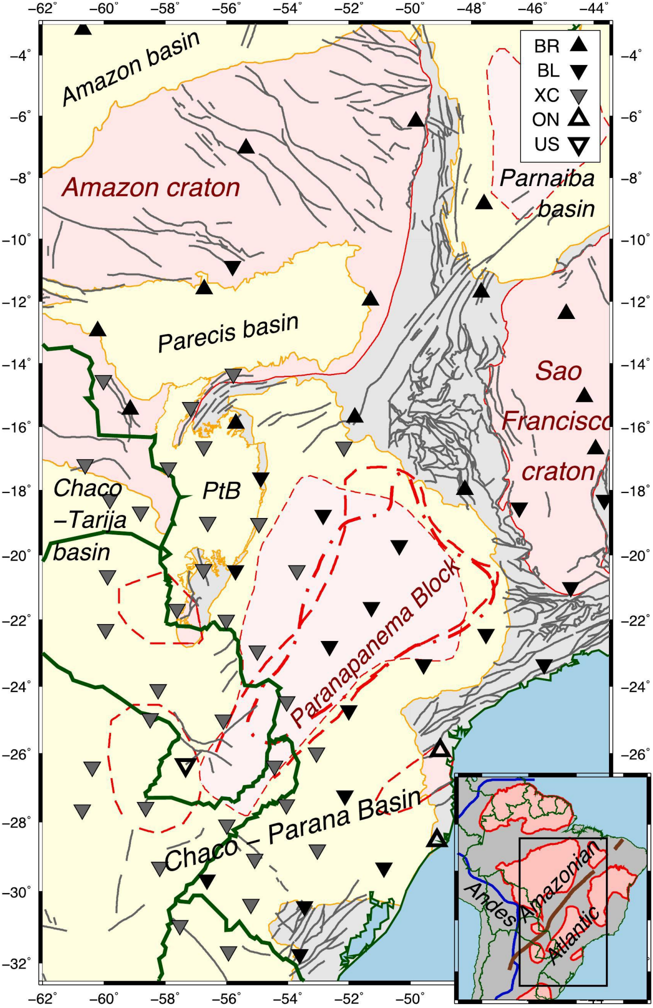

Amazon basin
Amazon craton
Parnaiba basin
Parecis basin
Sao Francisco craton
Chaco –Tarija basin
PtB
Paranapanema Block
Chaco – Parana Basin
BR
BL
XC
ON
US
Andes
Amazonian
Atlantic

Figure 1

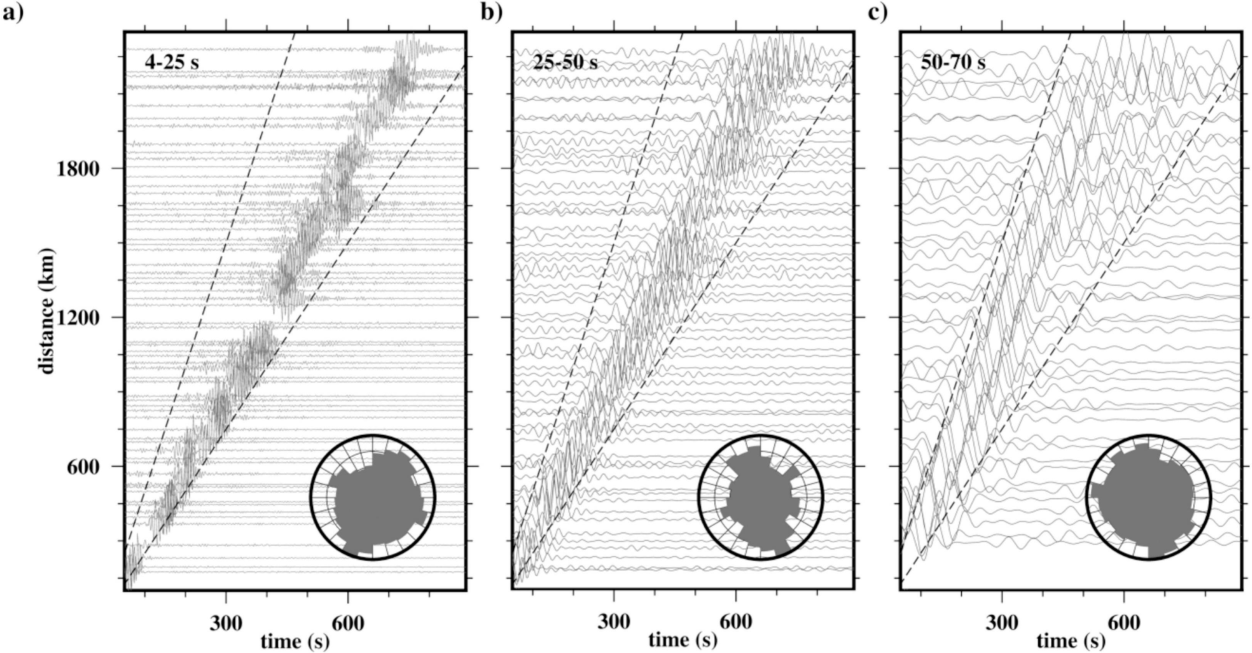

Figure 2

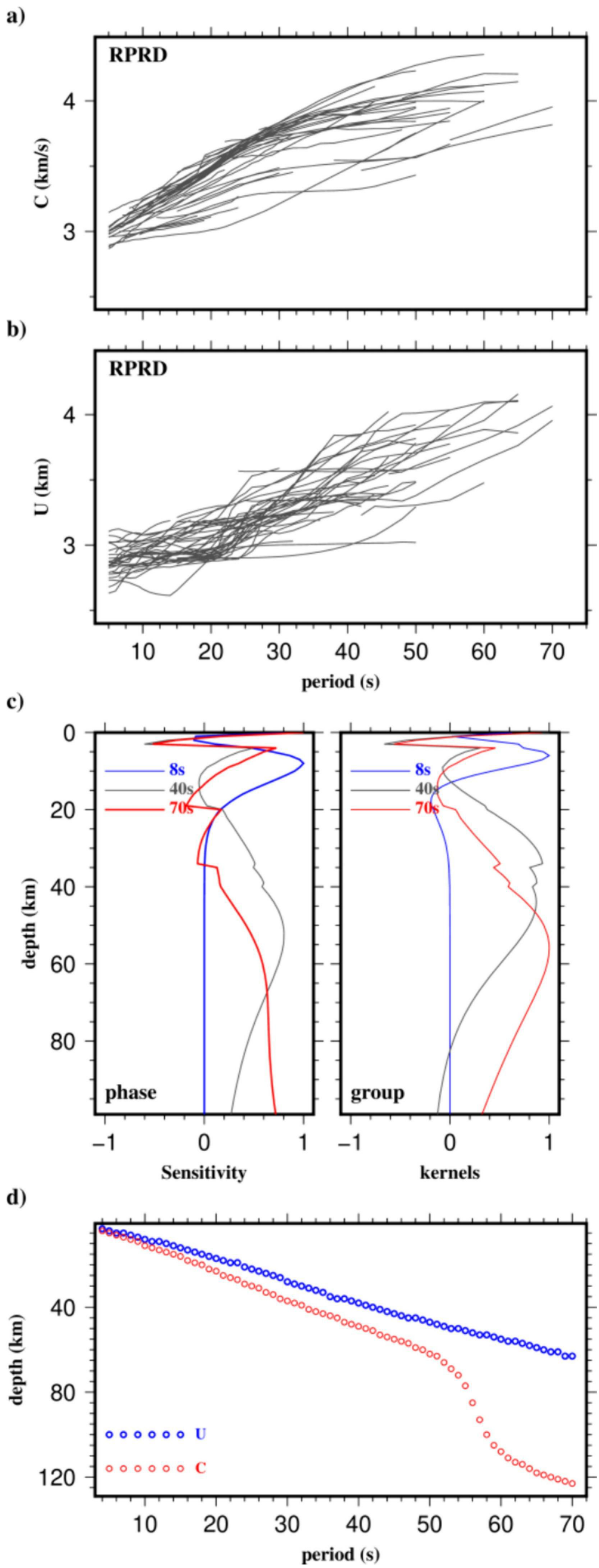

a)
RPRD
C (km/s)
4
3
b)
RPRD
U (km)
4
3
10
20
30
40
50
60
70
period (s)
c)
0
20
40
60
80
depth (km)
8s
40s
70s
phase
group
–1
0
1
Sensitivity
kernels
d)
40
80
120
depth (km)
U
C
10
20
30
40
50
60
70
period (s)

Figure 3

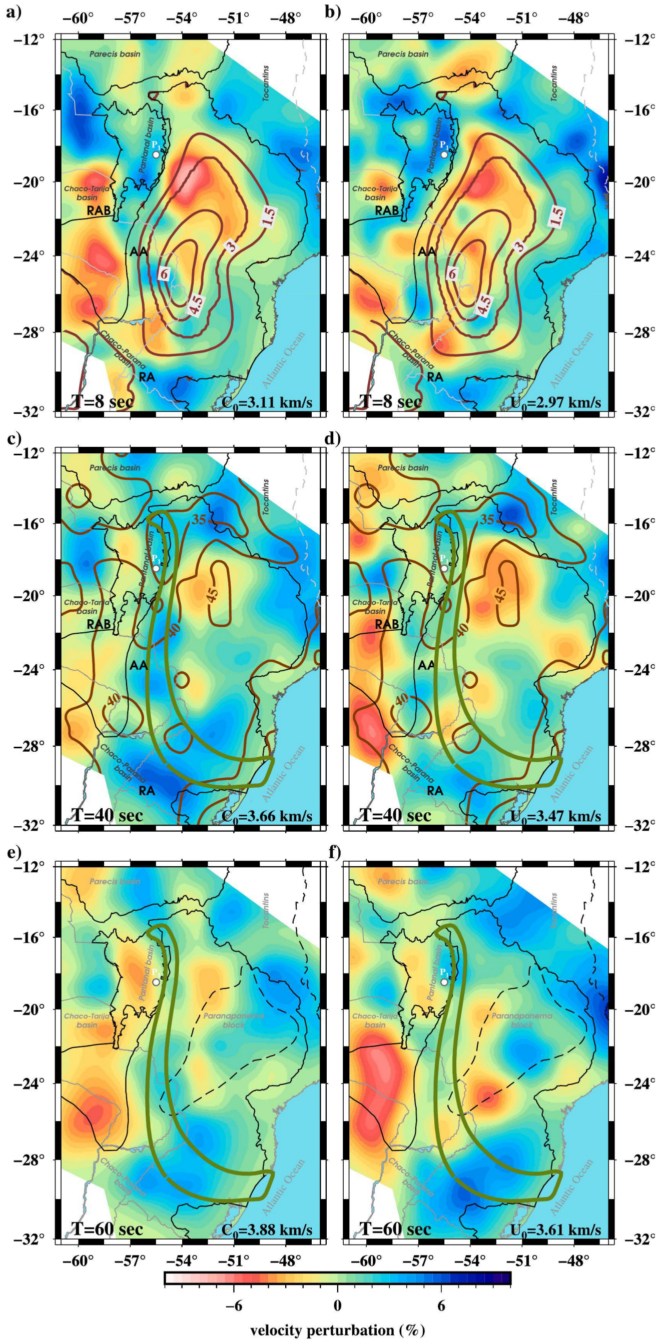

a)
b)
c)
d)
e)
f)
Parecis basin
Tocantins
Pantanal basin
P1
Chaco-Tarija basin
RAB
AA
Chaco-Parana basin
RA
Atlantic Ocean
Paranapanema block
T=8 sec
C0=3.11 km/s
U0=2.97 km/s
T=40 sec
C0=3.66 km/s
U0=3.47 km/s
T=60 sec
C0=3.88 km/s
U0=3.61 km/s
1.5
3
4.5
6
35
40
45
−60°
−57°
−54°
−51°
−48°
−12°
−16°
−20°
−24°
−28°
−32°
−6
0
6
velocity perturbation (%)

Figure 4

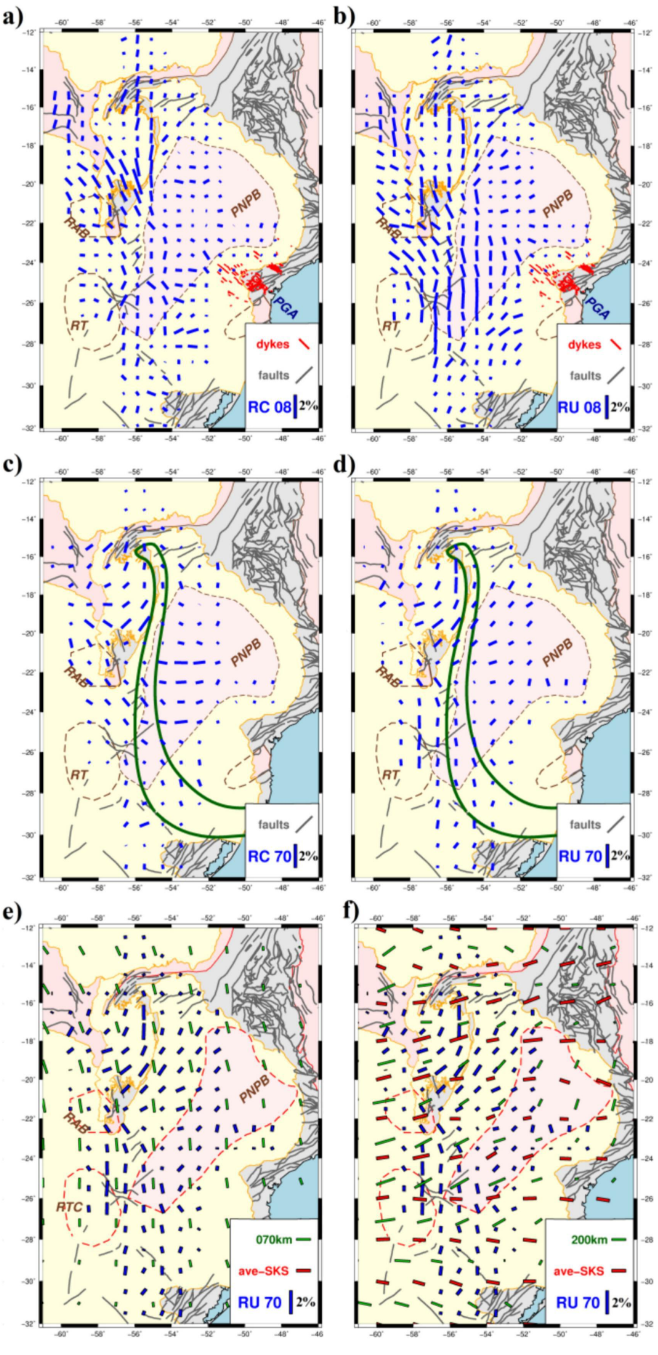
a)
b)
c)
d)
e)
f)
-60° -58° -56° -54° -52° -50° -48° -46°
-12° -14° -16° -18° -20° -22° -24° -26° -28° -30° -32°
PNPB
RAB
RT
RTC
PGA
dykes
faults
RC 08
RU 08
RC 70
RU 70
2%
070km
200km
ave–SKS

Figure 5

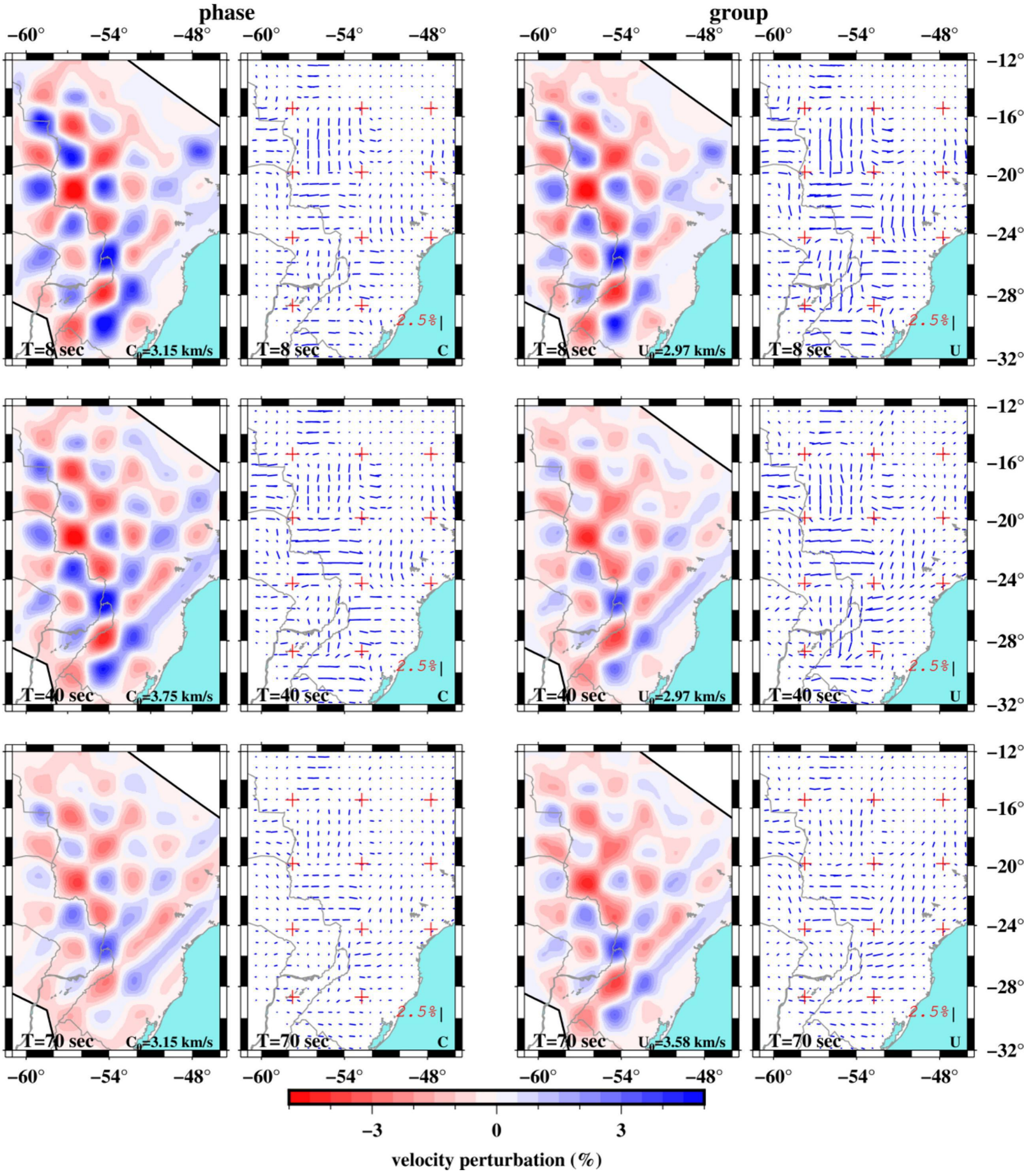
phase
group
T=8 sec
C_0=3.15 km/s
C
U_0=2.97 km/s
U
T=40 sec
C_0=3.75 km/s
U_0=2.97 km/s
T=70 sec
C_0=3.15 km/s
U_0=3.58 km/s
2.5%
−60°
−54°
−48°
−12°
−16°
−20°
−24°
−28°
−32°
−3
0
3
velocity perturbation (%)

Figure 6

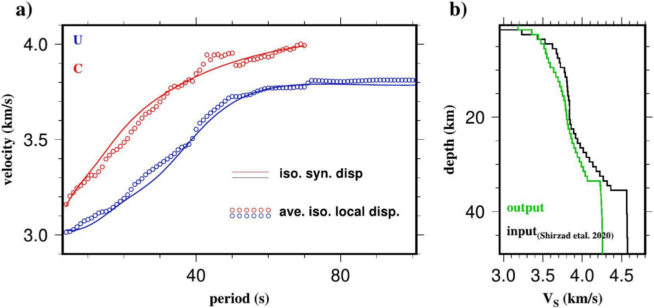

a)
U
C
4.0
3.5
3.0
velocity (km/s)
40
80
period (s)
iso. syn. disp
ave. iso. local disp.
b)
20
40
depth (km)
output
input(Shirzad etal. 2020)
3.0
3.5
4.0
4.5
V_S (km/s)

Figure 7

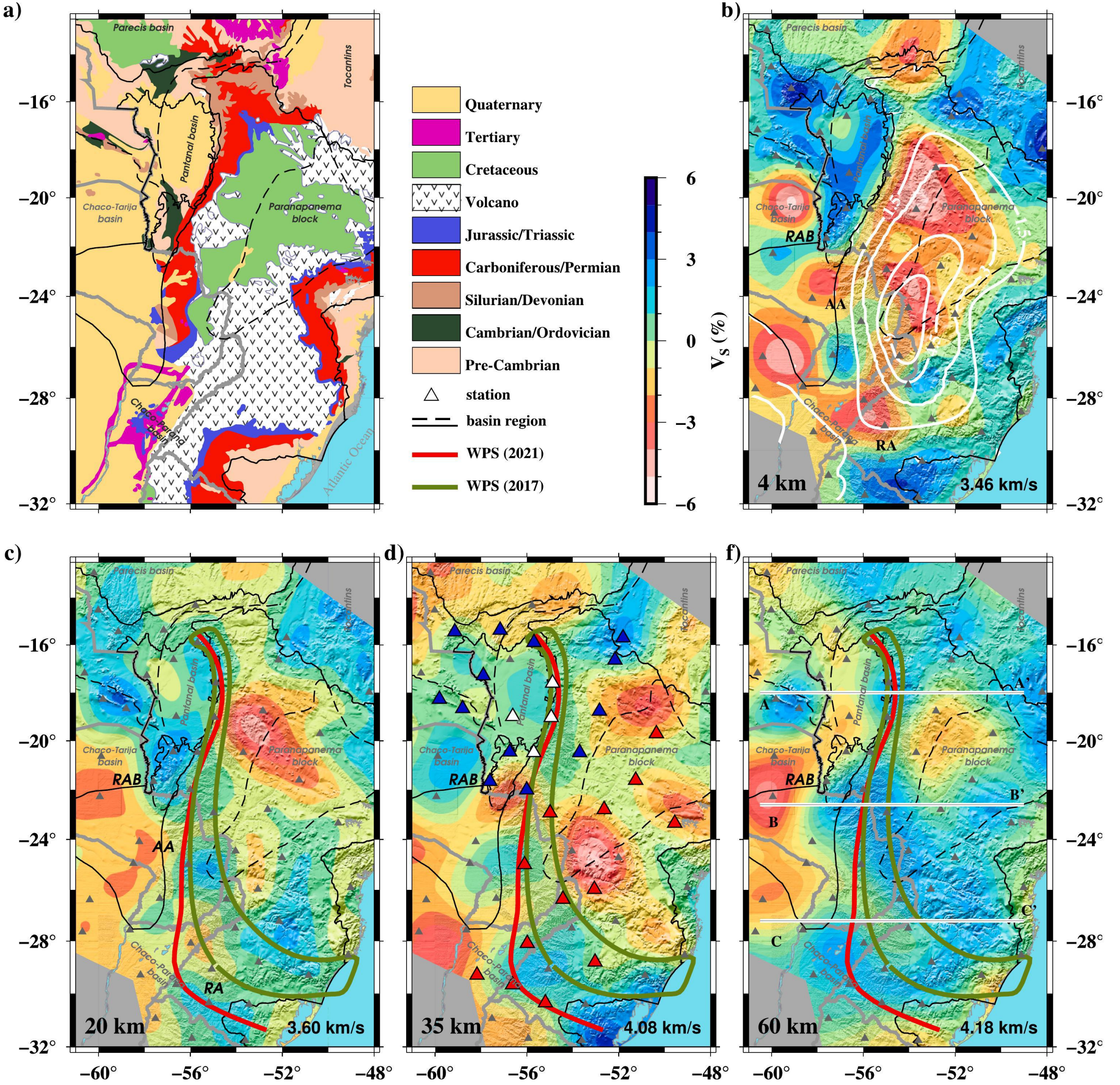
a)
b)
c)
d)
f)
Quaternary
Tertiary
Cretaceous
Volcano
Jurassic/Triassic
Carboniferous/Permian
Silurian/Devonian
Cambrian/Ordovician
Pre-Cambrian
station
basin region
WPS (2021)
WPS (2017)
V_S (%)
Parecis basin
Pantanal basin
Chaco-Tarija basin
Paranapanema block
Chaco-Paraná basin
Tocantins
Atlantic Ocean
RAB
AA
RA
A
A'
B
B'
C
C'
4 km
3.46 km/s
20 km
3.60 km/s
35 km
4.08 km/s
60 km
4.18 km/s

Figure 8

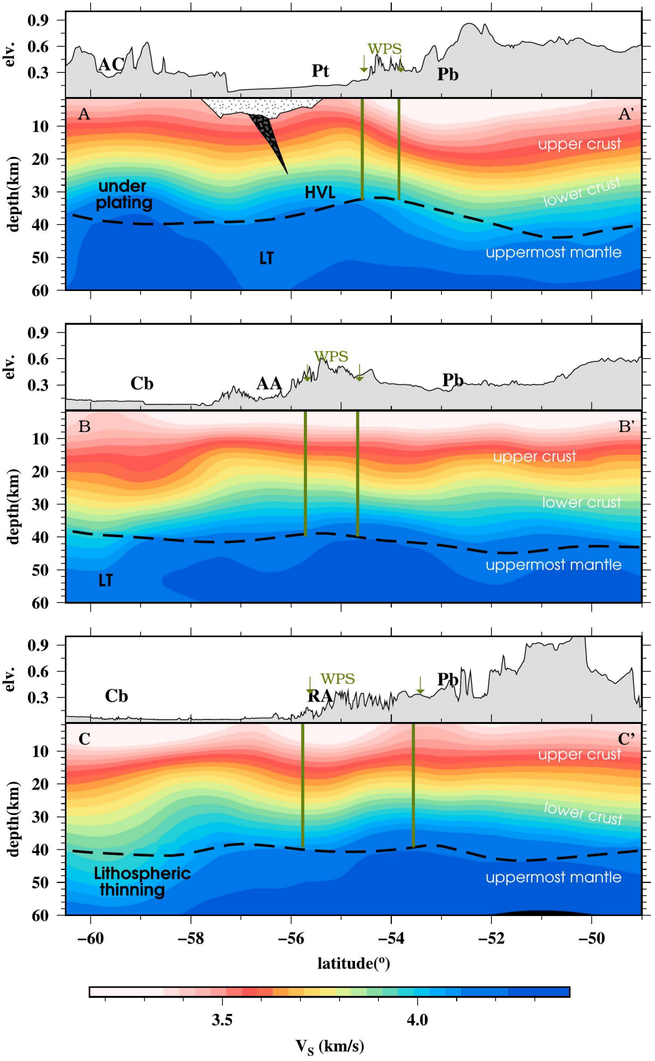

elv.
0.9
0.6
0.3
AC
Pt
WPS
Pb
A
A'
depth(km)
10
20
30
40
50
60
under plating
HVL
LT
upper crust
lower crust
uppermost mantle
Cb
AA
B
B'
C
C'
RA
Lithospheric thinning
-60
-58
-56
-54
-52
-50
latitude(°)
3.5
4.0
V_S (km/s)

Figure 9